EES Catalysis

Accepted Manuscript

Published on 09 September 2026

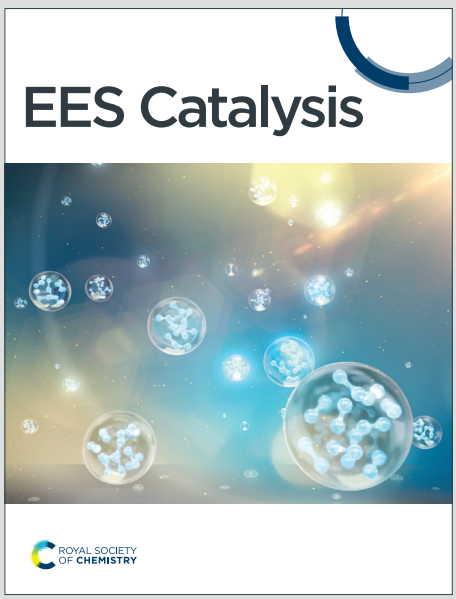

This is an Accepted Manuscript, which has been through the Royal Society of Chemistry peer review process and has been accepted for publication.

Accepted Manuscripts are published online shortly after acceptance, before technical editing, formatting and proof reading. Using this free service, authors can make their results available to the community, in citable form, before we publish the edited article. We will replace this Accepted Manuscript with the edited and formatted Advance Article as soon as it is available.

You can find more information about Accepted Manuscripts in the Information for Authors.

Please note that technical editing may introduce minor changes to the text and/or graphics, which may alter content. The journal's standard Terms & Conditions and the Ethical guidelines still apply. In no event shall the Royal Society of Chemistry be held responsible for any errors or omissions in this Accepted Manuscript or any consequences arising from the use of any information it contains.

ROYAL SOCIETY OF CHEMISTRY

Broader Context for

Improving the efficiency and lifespan of noble-metal-based catalysts is essential for reducing the cost and environmental impact of many energy-intensive chemical processes. Non-oxidative propane dehydrogenation (PDH), a key technology for on-demand propene production, heavily relies on platinum-based catalysts. While these catalysts contain a significant amount of platinum they are prone to progressive deactivation during repeated dehydrogenation and regeneration cycles. Efforts have been made to establish structure-activity relationships for developing active catalysts with lower platinum loading but relationships for designing durable catalysts remain largely unknown. This study identifies the platinum-oxygen-cobalt coordination number in bimetallic supported catalysts as a structural descriptor linking metal-metal interactions to catalyst durability. It demonstrates how platinum-cobalt interactions simultaneously enhance platinum utilisation and suppress structural degradation providing a mechanistic framework for designing highly efficient catalysts with reduced noble-metal consumption. Beyond propane dehydrogenation, the concept of using measurable interfacial coordination descriptors to guide catalyst design is expected to be broadly applicable to other high-temperature catalytic processes where catalyst stability and efficient use of critical raw materials are crucial.

Pt–(O)–Co Coordination Governs the Durability of Pt-Based Catalysts for Propane Dehydrogenation

Xiangnong Ding[a], Qiyang Zhang[a, *], Dmitry E. Doronkin[b], Tatiana Otroshchenko[a, *], Elizaveta Fedorova[a], Dongxu Wang[c], Stephan Bartling[a], Henrik Lund[a], David Linke[a], Evgenii V. Kondratenko[a, *]

[a]*Leibniz-Institut für Katalyse e.V., Albert-Einstein-Str. 29a, D-18059 Rostock, Germany.*

[b]*Institute for Chemical Technology and Polymer Chemistry, and Institute of Catalysis Research and Technology, Karlsruhe Institute of Technology, Kaiserstr. 12, D-76131, Karlsruhe, Germany.*

[c]*Max Planck Institute of Microstructure Physics, Weinberg 2, 06120 Halle, Germany.*

*To whom correspondence should be addressed. E-mail addresses: Qiyang.Zhang@catalysis.de (QZ); Tatiana.otroshchenko@catalysis.de (TO); Evgenii.kondratenko@catalysis.de (EVK)

Abstract

Non-oxidative propane dehydrogenation (PDH) has emerged as a promising technology for on-purpose propene production, but the Pt-based catalysts currently used are expensive and prone to sintering of platinum, which negatively affects their performance. Their activity can be restored by redispersing the active species after treatment in environmentally harmful Cl_2 or Cl-containing compounds. Herein, we demonstrate the application potential of Silicalite-1-supported Pt-Co bimetallic catalysts prepared by a simple impregnation method with a Pt loading of only 0.1 wt% and provide the origins of their high activity and especially durability. In terms of propene space-time yield related to the total amount of catalyst or platinum loading, the optimized 1Co0.1Pt/S-1 catalyst performed similarly to, or better than Pt-containing catalysts that had been previously developed and tested, albeit at higher temperatures. Another distinctive property of this catalyst is its high durability demonstrated in six dehydrogenation/regeneration cycles. The durability was found to increase progressively as the Co loading increases from 0 to 1 wt%. Comprehensive characterization revealed that the interaction strength between Pt and Co species, as reflected by the Pt–(O)–Co coordination number in the fresh catalysts, is the key factor governing catalyst durability. These findings provide valuable insights into the rational design of highly active and regenerable Pt-based dehydrogenation catalysts through the regulation of metal-metal interactions.

Keywords: propane dehydrogenation, Pt-Co bimetallic, synergistic effect, regeneration efficiency, silicalite-1.

Introduction

Propene is a key building block in the chemical industry and is widely used in the manufacture of various important products such as polypropylene, acrylic acid, and acetone [1-3]. Non-oxidative propane dehydrogenation (PDH) has emerged as one of the most promising on-purpose propene production methods, driven by the shale gas revolution and the growing demand for propene [2]. Pt-based catalysts have been widely used in PDH because of their high activity and selectivity for C–H bond activation, ensuring high propene selectivity [4-6]. However, they are expensive due to the high cost of Pt and inevitably suffer from deactivation caused by sintering of catalytically active Pt species and coke formation under industrially relevant conditions [5]. Although coke deposits can be removed upon oxidative catalyst treatment, repeated dehydrogenation/regeneration cycles often induce irreversible Pt aggregation and structural degradation, resulting in continuous loss of catalytic performance [7]. Therefore, developing cost-effective catalysts with reduced Pt loading, while simultaneously maintaining high activity and durability, i.e., the ability to restore the initial performance in a series of dehydrogenation/regeneration cycles, remains a long-standing challenge for industrial PDH catalysts [8].

An effective strategy for improving catalyst performance is to introduce a second metal (M) to construct highly dispersed Pt-M bimetallic species, such as Pt-Sn [9, 10], Pt-Ga [11, 12], Pt-In [13, 14], and Pt-Zn [15, 16]. These promoters can dilute Pt ensembles and modify the electronic properties of this metal, thereby improving catalytic activity and propene selectivity [17]. Nevertheless, previous studies have primarily focused on improving catalytic activity and selectivity, whereas considerably less attention has been devoted to understanding how the interaction between Pt and promoter metals influences catalyst durability [10, 13].

Among various Pt-M-based catalysts, those containing platinum and cobalt have been relatively under-explored [17-19]. Miller et al. prepared a series of $CoPt/SiO_2$ samples and found that Co diluted large Pt surface ensembles, leading to the formation of Pt_3Co surface structures that are responsible for efficient propane dehydrogenation [17]. However, their durability was not investigated. On the other hand, Li et al. synthesized Co//Pt bimetallic catalysts by integrating spatially separated Co and Pt metal centers in/on nitrogen-doped carbon (NC) supports [20]. The most promising sample provided a low deactivation rate (0.0036 h^{-1}) and high propene selectivity when H_2 was present in the reaction feed. However, the selectivity decreased markedly in the absence of H_2. Recently, our group developed a bimetallic 1Co-0.1Pt@Silicalite-1(S-1) catalyst with only 0.1 wt% Pt via hydrothermal synthesis, which

exhibited high activity and on-stream stability in the PDH reaction [8]. The in situ formation of sub-nanosized PtCo intermetallic compounds confined within the S-1 zeolite was identified as the origin of its outstanding catalytic performance. However, the catalysts developed gradually lost their initial high activity after repeated oxidative regeneration because of Pt agglomeration. Collectively, these studies demonstrate the considerable potential of Pt-Co catalysts for efficient propane dehydrogenation, while also revealing that catalyst durability remains a critical challenge.

Given the above context, this study aimed to explore whether and how Pt-Co interactions within bimetallic particles influence their structural stability through repeated dehydrogenation and oxidative regeneration cycles. To achieve this, a series of Pt-Co-containing catalysts (xCo0.1Pt/S-1) were prepared using the attractive, from an application point of view, incipient wetness impregnation method. S-1 was selected as the support because its purely siliceous framework provides a relatively inert and weakly acidic environment, which minimizes support-induced side reactions and facilitates the investigation of the intrinsic interaction between Pt and Co species. These catalysts have a fixed Pt content of just 0.1 wt% and varied Co loadings. Comprehensive characterization analyses and density functional theory (DFT) calculations reveal a pronounced synergistic interaction between Pt and Co species, whereby the presence of Co maintains Pt species in an oxidized state, in contrast to the metallic state in the monometallic 0.1Pt/S-1 catalyst. Meanwhile, Pt facilitates the reduction of CoO_x species. This synergistic interaction gives rise to highly active Pt-Co species for efficient propane dehydrogenation. More importantly, we show that the strength of the Pt-Co interactions is crucial for stabilizing the bimetallic species against restructuring during a series of dehydrogenation and regeneration cycles. As the Co loading increased from 0 to 1 wt%, the Pt–(O)–Co coordination number increased progressively and exhibited a strong positive correlation with catalyst regeneration efficiency, establishing the Pt–(O)–Co coordination number in the fresh catalysts as a structural descriptor that correlates the local Pt-Co interaction with regeneration durability within this series of Pt-Co/S-1 catalysts.

Experimental Methods

Catalyst synthesis

Tetraethyl orthosilicate (TEOS, Sigma-Aldrich), Cobalt(II) nitrate hexahydrate ($Co(NO_3)_2 \cdot 6H_2O$, 99.0%, Sigma-Aldrich), Tetrapropylammonium hydroxide (TPAOH, 1 M in

water, Thermo Scientific), Tetraammineplatinum(II) nitrate ($[Pt(NH_3)_4](NO_3)_2$, ≥50.0% Pt basis, Sigma-Aldrich) were used as starting materials. The chemicals were used as received.

Silicalite-1 (S-1) was synthesized according to our previous work but with some modifications [21]. TEOS, TPAOH, and deionized water were mixed at a molar ratio of TEOS:TPAOH:H_2O = 1:0.2:15 and then stirred at room temperature for 6 h. The resulting clear solution was transferred into a stainless-steel autoclave and hydrothermally treated at 190 °C for 48 h. After cooling to room temperature, the solid product was recovered by centrifugation, washed five times with deionized water, and calcined in air at 550 °C for 6 h to obtain the S-1 support.

A series of CoPt-containing catalysts with a Pt loading of 0.1 wt% and a Co loading ranging from 0.1 to 2 wt% were prepared by incipient wetness impregnation. The S-1 support was impregnated with an aqueous solution of $Co(NO_3)_2 \cdot 6H_2O$ and $[Pt(NH_3)_4](NO_3)_2$, and then left to stand overnight. The resulting solids were then dried at 100 °C for 12 h and calcined in air at 550 °C for 2 h. The obtained samples were denoted as xCo0.1Pt/S-1, where "x" represents the Co loading (wt%). The reference monometallic Co-free 0.1Pt/S-1 and Pt-free xCo/S-1 catalysts were prepared following the same procedure used for the preparation of the xCo0.1Pt/S-1 catalysts without adding $Co(NO_3)_2 \cdot 6H_2O$ or $[Pt(NH_3)_4](NO_3)_2$, respectively.

Catalyst characterization

X-ray diffraction (XRD) patterns of all catalysts were collected on a Panalytical X'Pert θ/2θ-diffractometer equipped with X'celerator detector, using Cu $K_{\alpha 1/\alpha 2}$ radiation (40 kV, 40 mA, λ = 0.15406 nm and 0.15444 nm). The Cu K_β radiation was removed using a nickel filter.

Transmission electron microscopy (TEM) analysis was performed on an FEI Talos 200X microscope operating at an accelerating voltage of 200 kV. Aberration-corrected scanning transmission electron microscopy (AC-STEM) and elemental mapping tests were performed on an FEI Titan Cubed Themis G2 microscope operating at 300 kV to characterize the microstructure and elemental distribution of the prepared catalysts.

The as-prepared catalysts were characterized by diffusion-reflection UV-vis spectroscopy using an Avantes spectrometer (AvaSpec-2048-USB2-RM) equipped with a high-temperature reflection probe, an AvaLight-DH-S-BAL deuterium-halogen light source, and a CCD array detector. $BaSO_4$ (99.998%, Aldrich) was used as a white standard. The spectra were collected at room temperature in the range of 200-1100 nm.

X-ray photoelectron spectroscopy (XPS) analysis was carried out on a Thermo Fisher ESCALAB 220iXL instrument with monochromatic Al Kα radiation (E = 1486.6 eV). The samples were mounted on a stainless-steel sample holder using conductive double-sided carbon tape. Charge neutralization during the measurements was achieved by a flood electron system combining low energy electrons and Ar^+ ions ($p_{Ar} = 1\times10^{-7}$ mbar). The binding energies were referenced to the C 1s peak at 284.8 eV assigned to adventitious carbon (C–C or C–H). Quantitative analysis was performed by fitting the spectra with mixed Gaussian–Lorentzian functions using the Unifit 2023 software package. The peak areas were normalized using the spectrometer transmission function and Scofield element-specific sensitivity factors.

As-prepared catalysts were characterized by X-ray absorption spectroscopy (XAS) at the Pt L_3-edge using the P65 beamline of the PETRA III synchrotron radiation source (DESY, Hamburg). Higher harmonics were rejected by a pair of Si plane mirrors installed in front of the monochromator. The energy of the X-ray photons was further selected by a Si(111) double-crystal monochromator and the beam size was set by means of slits to 0.4 (vertical) x 2.0 (horizontal) mm^2. Pt L_3-edge spectra were recorded using a large area 4-element silicon drift detector (2 mm thick Hitachi Vortex®-ME4) coupled with XGLab DANTE digital pulse processor. The spectra were recorded in continuous mode while the scanning incident energy varied from -150 eV to +800 eV relative to the respective absorption edge. They were normalized, and the extended X-ray absorption fine structure (EXAFS) spectra background was subtracted using the ATHENA program from the IFEFFIT software package [22]. The k^2-weighted EXAFS functions were Fourier transformed (FT) over the k range of 3.0-10.0 $Å^{-1}$ using a Hanning window with a sill width of 1 $Å^{-1}$. The FT EXAFS spectra were not corrected for the phase shift. The fitting was performed in the r-space on k^1, k^2-weighted data in the r-range of 1.2-3.0 Å. During the EXAFS spectra fitting, structural parameters for different shells were refined in an iterative manner while fixing the corresponding parameters for the neighboring shells. Pt foil was used as reference to determine the reduction factor (S_0^2) for fitting at the Pt L_3-edge.

N_2 adsorption-desorption isotherms of all samples were collected in a Belsorp-max II setup (Microtrac-BEL) at -196 °C. Prior to the measurements, the catalysts were degassed under vacuum at 250 °C for 2 h. The specific surface area was calculated using the Brunauer–Emmett–Teller (BET) method, and the total pore volume was determined at a relative pressure (P/P_0) of 0.99.

O_2 pulse experiments were performed at ambient pressure to investigate the redox properties of the reduced catalysts as follows. Firstly, 100 mg of each catalyst were heated to 550 °C in a flow of air (20 mL min^{-1}), and then flushed with He for 10 min. Subsequently, the catalysts were reduced in a flow of 50 vol% H_2/He (20 mL min^{-1}) for 30 min to ensure complete reduction. After flushing with He for 15 min, an O_2/Ar (1/49, vol/vol) mixture was pulsed five times with a pulse size of 1 mL to re-oxidize the reduced metallic Co and/or Pt species. The signals at m/z = 32 (O_2), 2 (H_2), 18 (H_2O), and 40 (Ar) were recorded using an on-line mass spectrometer (Pfeiffer Vacuum OmniStar GSD 350). The reduction degree of CoO_x (Re(Co)) after the above-described catalyst treatment in H_2 was calculated according to equation (1):

$$\mathrm{Re(Co)} = 1 - \frac{v_{Co} \times n_{Co} - 4 \times n_{O2}}{2 \times n_{Co}} \quad (1)$$

,where v_{Co} is the average oxidation state of Co in the fresh sample, which is +2 in the present case. n_{Co} stands for the mole amount of Co in the fresh sample, and n_{O2} stands for the mole amount of O_2 consumed during the O_2 pulse titration. The n_{O2} value was obtained by subtracting the amount of O_2 consumed by 0.1Pt/S-1 from the amount consumed by a certain xCo0.1Pt/S-1 catalyst.

Catalytic tests

Catalytic tests were carried out in an in-house-developed setup consisting of 15 continuous-flow fixed-bed quartz reactors with an outer diameter of 6 mm and an inner diameter of 4 mm. The rate of propene formation ($r(C_3H_6)$) was determined after 300 s on stream according to equation (2), with propane conversion maintained below 10%. Typically, each catalyst (5 or 10 mg, 315-710 μm) was loaded in the middle of the reactor (a 1 cm layer of SiC was placed on top of the catalyst bed to ensure plug flow and preheat the feed components) and then preheated to 550 °C in a N_2 flow with a heating rate of 10 °C min^{-1}. Hereafter, a flow of 40 vol% C_3H_8/N_2 (80 or 20 mL min^{-1}) was introduced into the reactor.

To determine the apparent activation energy (E_a) of propene formation, catalytic tests were performed in the temperature range of 425-510 °C, in which the catalyst amount (5-30 mg) and the total feed flow rate (10-80 mL min^{-1}) were varied to maintain propane conversion below 10%.

The durability tests consisted of a series of PDH and oxidative regeneration cycles at 550 °C using a feed of 40 vol% C_3H_8 in N_2 with a total flow rate of 20 mL min^{-1} and air with a total flow of 15 mL min^{-1}, respectively. The catalyst amount was set to 20 mg for xCo0.1Pt/S-

1 or 75 mg for 0.1Pt/S-1. Each cycle included the following steps: (i) propane dehydrogenation for 60 min; (ii) N_2 flushing for 10 min; (iii) oxidation in air at the same temperature for 10 min to remove carbon deposits; and (iv) purging with N_2 for 10 min.

To compare the different catalysts with respect to their time-on-stream activity and stability, additional tests were carried out using 20 mg of each catalyst. The catalysts were initially heated to 550 °C with a rate of 10 °C min^{-1} in an N_2 flow. Then, they were tested for their PDH activity in a reaction mixture containing 40 vol% C_3H_8 in N_2 (20 mL min^{-1}). Propane conversion ($X(C_3H_8)$), propene selectivity ($S(C_3H_6)$), space-time yield of propene formation related to the total amount of catalyst ($STY(C_3H_6)_{cat}$) or to the amount of Pt ($STY(C_3H_6)_{Pt}$)), and apparent catalyst deactivation rate constant (k_d) were calculated according to equations (3–7), respectively.

$$r(C_3H_6) = \frac{\dot{n}^{out}_{C_3H_6}}{m_{cat}} \quad (2)$$

$$X(C_3H_8) = \frac{\dot{n}^{in}_{C_3H_8} - \dot{n}^{out}_{C_3H_8}}{\dot{n}^{in}_{C_3H_8}} \quad (3)$$

$$S_i = \frac{\nu_{C_3H_8}}{\nu_i} \times \frac{\dot{n}_i^{out}}{\dot{n}^{in}_{C_3H_8} - \dot{n}^{out}_{C_3H_8}} \quad (4)$$

$$STY(C_3H_6)_{cat} = \frac{F_{feed} \times \chi_{(C_3H_6)} \times M_{(C_3H_6)}}{1000 \times V_m \times m_{cat}} \quad (5)$$

$$STY(C_3H_6)_{Pt} = \frac{STY(C_3H_6)}{M_{(C_3H_6)} \times W_{Pt}} \quad (6)$$

$$k_d = \frac{\ln \frac{1-X_{end}}{X_{end}} - \ln \frac{1-X_{initial}}{X_{initial}}}{t} \quad (7)$$

$\dot{n}_i$ with superscripts in or out stands for the molar flow of gas-phase components at the reactor inlet or outlet. ν_i is the stoichiometric coefficient for product i. F_{feed} is the total feed flow rate. $\chi(C_3H_6)$ stands for the mole fraction of propene at the reactor outlet, while m_{cat} is the catalyst mass. W_{Pt} represents the Pt amount in the catalyst. $X_{initial}$ and X_{end} stand for propane conversion after 5 min and 12 h on stream, respectively.

An on-line gas chromatograph (Agilent 6890) equipped with PLOT/Q (for CO_2), Al_2O_3/S (for hydrocarbons), and molecular sieve 5A (for H_2, O_2, N_2, and CO) columns, as well as flame ionization (FID) and thermal conductivity (TCD) detectors, was used to quantify the reactants (C_3H_8, N_2) and reaction products (C_3H_6, CH_4, H_2, etc.).

DFT calculations

All spin-polarized periodic density functional theory (DFT) calculations were performed using the Vienna ab initio simulation package (VASP) with the Perdew-Burke-Ernzerhof (PBE) exchange-correlation functional [23] and the projector-augmented wave (PAW) method [24, 25]. An energy cutoff of 500 eV was applied. Geometry optimization was converged until the forces acting on the atoms were lower than 0.02 eV $Å^{-1}$. The energy threshold defining self-consistency of the electron density was set to 10^{-5} eV. Gaussian smearing with a width of 0.05 eV was used. The Brillouin zone sampling was restricted to the Γ-point. The clusters were placed at the center of a supercell of size 40 × 40 × 40 $Å^3$, large enough to ensure negligible interaction between periodic images.

To investigate the ability of Pt atoms to aggregate, small Pt clusters (Pt_2, Pt_3, Pt_6, and Pt_{13}) were constructed by extracting finite fragments from bulk cubic Pt and were fully optimized. The stability of these clusters was evaluated using the average energy per Pt atom, defined in equation (8).

$$E_n^{avg} = \frac{E(Pt_n)}{n} \quad (8)$$

where $E(Pt_n)$ is the total energy of the Pt_n cluster and n is the number of Pt atoms. More negative values of E_n^{avg} for larger n indicate higher stability and therefore a stronger tendency of Pt toward aggregation.

The interaction of PtO_2 with the $Co_{12}O_{12}$ cluster was investigated to evaluate its tendency to bind to and incorporate into this cluster. The $Co_{12}O_{12}$ cluster was selected as a model of the CoO_x species based on experimental characterization data. XPS and UV-vis results show that Co is predominantly present as Co^{2+} in the as-prepared catalysts, while no spectral features attributable to bulk Co_3O_4 were observed. In addition, TEM images show that the CoO_x species are highly dispersed, with only a very limited number of small clusters observed for the bimetallic 1Co0.1Pt/S-1 catalyst. The $Co_{12}O_{12}$ cluster has a size of approximately 0.6 nm and therefore provides a reasonable model for the small, highly dispersed CoO_x species observed experimentally. Cluster models were constructed for $Co_{12}O_{12}$ and PtO_2 by extracting finite stoichiometric fragments from their respective bulk structures (cubic CoO and tetragonal PtO_2). First, the isolated $Co_{12}O_{12}$ and PtO_2 clusters were fully optimized. Subsequently, three composite configurations were investigated: (i) PtO_2 adsorbed on the $Co_{12}O_{12}$ cluster surface, (ii) PtO_2 incorporated into the surface region of the $Co_{12}O_{12}$ cluster, and (iii) PtO_2 incorporated into the bulk region of the $Co_{12}O_{12}$ cluster. All configurations were fully relaxed under the same

computational conditions. The tendency of PtO_2 to bind to or incorporate into the $Co_{12}O_{12}$ cluster was quantified by the formation energy, defined as:

$$\Delta E_f = E(Co_{12}O_{12} \text{ with } PtO_2) - E(Co_{12}O_{12}) - E(PtO_2) \quad (9)$$

where $E(Co_{12}O_{12} \text{ with } PtO_2)$ is the total energy of the combined system, $E(Co_{12}O_{12})$ and $E(PtO_2)$ correspond to the isolated optimized $Co_{12}O_{12}$ and PtO_2 clusters. More negative values of ΔE_f indicate a more thermodynamically favorable interaction, corresponding to binding or incorporation of PtO_2 into the $Co_{12}O_{12}$ cluster.

Finally, the effect of Pt incorporation into the $Co_{12}O_{12}$ cluster on the reducibility of the latter was investigated. To this end, the formation energy of an oxygen vacancy was calculated for different oxygen positions in the pristine $Co_{12}O_{12}$ cluster and in the system where PtO_2 is incorporated into the surface region of $Co_{12}O_{12}$. The oxygen vacancy formation energy was calculated according to equation (10):

$$\Delta E_f = E(\text{cluster with vacancy}) + \frac{1}{2}E(O_2) - E(\text{cluster}) \quad (10)$$

where $E(\text{cluster with vacancy})$ is the total energy of the defective cluster after removing an oxygen atom, $E(\text{cluster})$ is the energy of the pristine cluster, and $E(O_2)$ is the total energy of an isolated oxygen molecule in a box of $40 \times 40 \times 40$ Å^3. Lower values of ΔE_f indicate more favourable oxygen removal and therefore higher reducibility of the system.

Results and discussion

Platform of catalysts and their physicochemical characteristics

The XRD patterns of all catalysts exhibited the characteristic diffraction peaks of the MFI framework (Fig. 1a and Fig. S1, PDF#01-070-4743). No crystalline bulk Co- and/or Pt-containing phases were identified in the obtained XRD patterns of the xCo0.1Pt/S-1, 0.1Pt/S-1 and xCo/S-1 catalysts. The catalysts exhibit a typical I N_2 adsorption-desorption isotherm, characteristic of microporous materials (Fig. 1b, Fig. S2 and Table S1) [26]. The specific surface area of the parent S-1 support decreased after the introduction of Pt and/or Co species and further decreased with increasing Co loading (from 497 to 395 $m^2\ g^{-1}$). The UV-vis spectra of the 1Co/S-1 and xCo0.1Pt/S-1 catalysts exhibit two absorption bands at approximately 580 and 650 nm, which can be assigned to the $^4A_2 \rightarrow {}^4T_1(P)$ transitions of tetrahedral Co^{2+} species (Fig. 1c) [27, 28]. In contrast, no absorption bands attributed to bulk Co_3O_4 species (typically located

approximately at 450 and 720 nm) were observed, suggesting that the Co species are highly dispersed on the S-1 support [29].

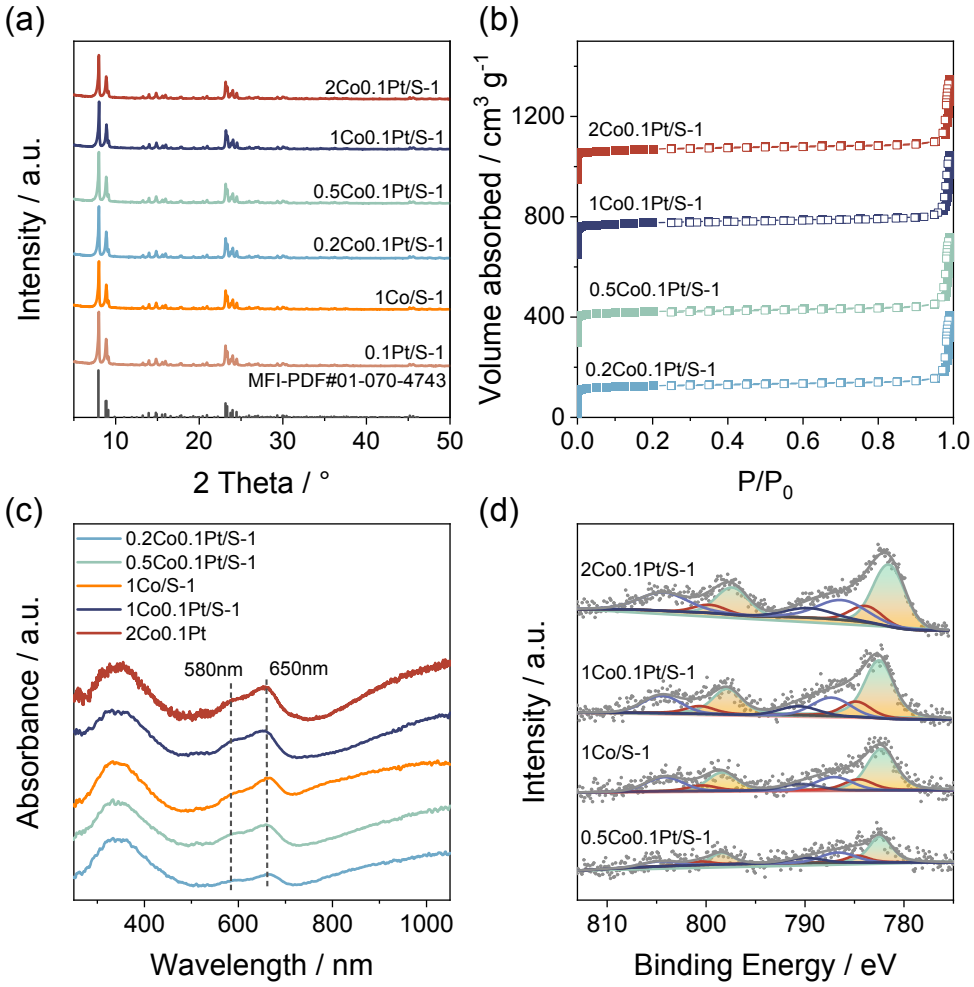

Fig. 1 (a) XRD patterns, (b) N_2 adsorption-desorption isotherms, (c) UV-vis and (d) Co 2p XP spectra of the as-prepared catalysts.

The Co 2p XP spectra of the as-prepared catalysts in Fig. 1d are characterized by two main signals at the binding energies of approximately 782.2 eV and 798.2 eV, which can be attributed to Co $2p_{3/2}$ and Co $2p_{1/2}$, respectively [28, 30, 31]. Moreover, the presence of characteristic satellite peaks at 787.1 eV and 804.2 eV suggests that Co is predominantly present as Co^{2+}. The Pt 4f region of the monometallic 0.1Pt/S-1 catalyst (Fig. S3) is characterized by two main signals at the binding energies of approximately 71.4 eV and 74.9 eV attributed to the Pt $4f_{7/2}$ and Pt $4f_{5/2}$ of metallic Pt^0, respectively [32]. The weak signals observed at about 74.0 eV and 77.5 eV can be attributed to Pt^{2+} species [33]. Therefore, Pt is predominantly present in the metallic state in the 0.1Pt/S-1 catalyst. For the bimetallic catalysts, no distinct Pt signal could be identified owing to the low Pt concentration at the surface.

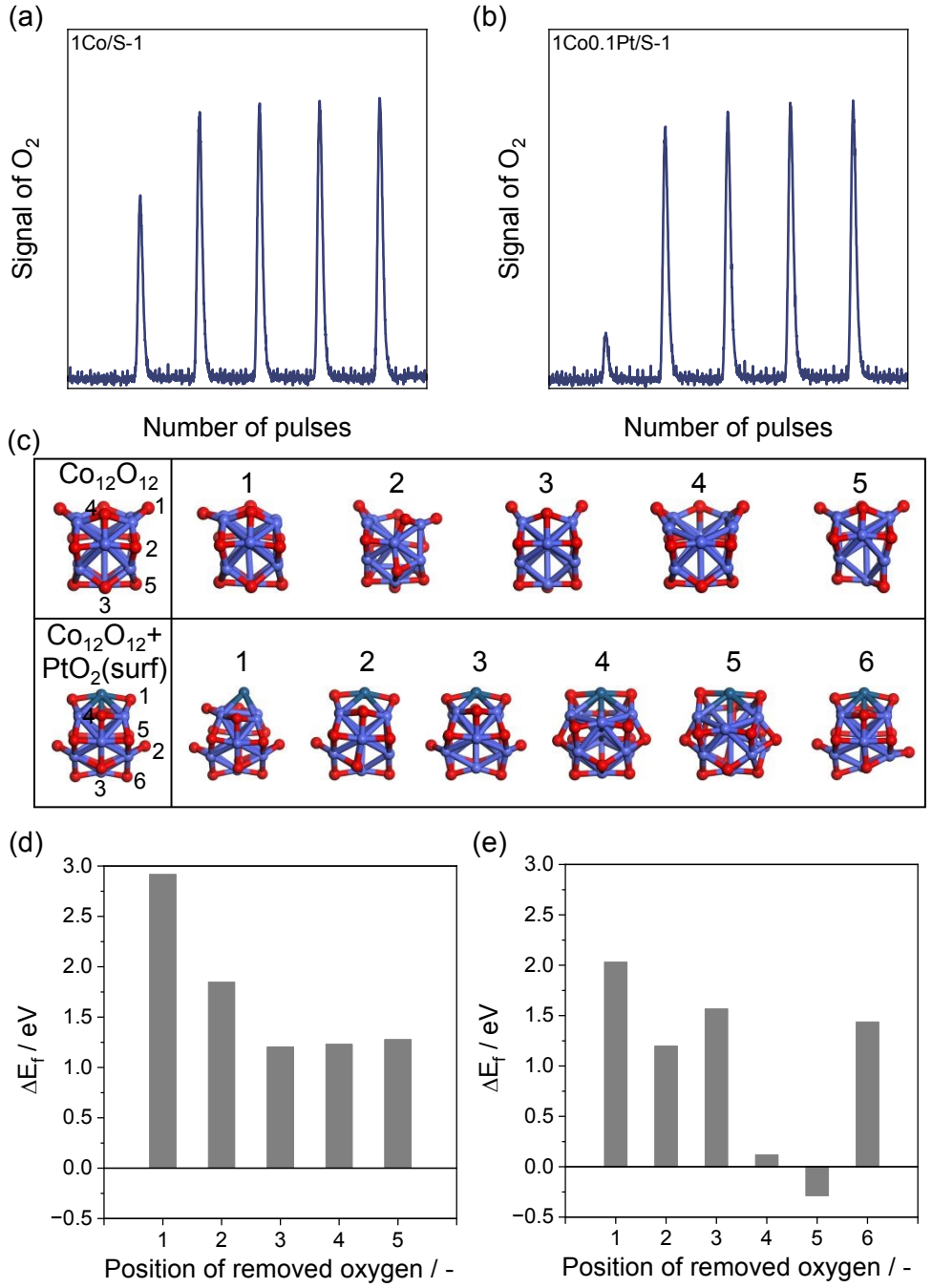

Fig. 2 The O_2 outlet signals after pulsing (1mL) of an O_2/Ar = 1/49 mixture over (a)1Co/S-1 and (b) 1Co0.1Pt/S-1 at 550°C. Before the O_2 pulses, the catalysts were exposed to a flow of H_2/Ar = 1/1 (20 mL min^{-1}) at 550 °C for 30 min and then flushed with He (20 mL min^{-1}) for 15 min. (c) Structures of $Co_{12}O_{12}$ and $Co_{12}O_{12}$+PtO_2(surf) clusters showing the positions of removed oxygen atoms and the corresponding optimized structures after oxygen removal. Oxygen vacancy formation energy for different oxygen sites in (d) $Co_{12}O_{12}$ and (e) $Co_{12}O_{12}$+ PtO_2(surf) clusters.

To determine the reduction degree of CoO_x in the 1Co/S-1 and 1Co0.1Pt/S-1 catalysts, we performed O_2 pulse titration experiments at 550°C (Fig. 2a-b and Fig. S4). The catalysts

were pre-reduced in a flow of H_2/Ar = 1/1 (20 mL min^{-1}) at the same temperature for 30 min. The fraction of metallic Co in the reduced 1Co/S-1 catalyst is about 5%, which is significantly lower than the 29% observed for the reduced bimetallic 1Co0.1Pt/S-1 catalyst. This result indicates that the presence of Pt species promotes the reduction of CoO_x species, confirming the synergistic interaction between Co and Pt species. The enhanced reducibility of CoO_x in the presence of Pt can be attributed to both hydrogen activation by Pt and modification of the local Co-O environment. Pt is highly active for H_2 dissociation, and the resulting hydrogen species can migrate to neighboring CoO_x species through hydrogen spillover, facilitating their reduction. To gain molecular level insight into this synergistic effect, DFT calculations were performed. The effect of PtO_2 incorporation into the $Co_{12}O_{12}$ cluster on the reducibility of the latter was evaluated by calculating the oxygen vacancy formation energy for different oxygen positions in the cluster (Fig. 2c). For the pristine $Co_{12}O_{12}$ cluster, the vacancy formation energy ranges from 1.2 to 2.9 eV (Fig. 2d), indicating that oxygen removal is unfavorable and depends on the local Co environment. For the $Co_{12}O_{12}$ cluster with PtO_2 incorporated into the surface region, a broader range of vacancy formation energy was obtained, from -0.3 to 2.0 eV (Fig. 2e). Notably, the presence of Pt significantly lowers the energy for certain positions, particularly for oxygen atoms located near the incorporated Pt species. This indicates that Pt facilitates oxygen removal at specific sites, thereby enhancing the reducibility of the $Co_{12}O_{12}$ cluster, further supporting the results obtained from O_2 titration experiments. As identified in our previous studies, the reducibility of CoO_x plays an essential role in the activity of different monometallic Co-containing catalysts ref. [29, 34].

XAS measurements were conducted to gain a deeper understanding of the local structure of Pt in mono- and bimetallic catalysts (Fig. 3). The features in the XANES spectrum of the 0.1Pt/S-1 catalyst are similar to those of Pt foil, indicating that Pt is predominantly present in its metallic state, in good agreement with the XPS result (Fig. 3a). The XANES features of bimetallic catalysts (xCo0.1Pt/S-1) progressively approach those of PtO_2 with increasing Co loading from 0.2 to 0.5 wt%. The white-line intensity increases with increasing Co loading up to 1 wt% and then remains nearly constant, suggesting that the oxidation state of Pt increases with increasing Co loading from 0.2 to 1 wt%. Given the fixed Pt loading of 0.1 wt%, the progressive increase in Co loading promotes the interaction of Pt species with CoO_x, resulting in a gradual increase in the oxidized character of Pt. At approximately 1 wt% Co, the oxidation state of Pt appears to approach a plateau, as reflected by the nearly constant white-line intensity upon further increasing the Co loading. These results reveal that Pt predominantly exists in oxidized states (Pt^{n+}) in the presence of CoO_x species, in sharp contrast to the metallic Pt^0

observed in the 0.1Pt/S-1 catalyst. These observations clearly demonstrate that the local structure and electronic state of Pt are strongly affected by interactions with CoO_x species, whose presence favors the formation and stabilization of Pt^{n+} species. Furthermore, the varying structural and electronic characteristics reflect different interaction strengths between Pt and Co species.

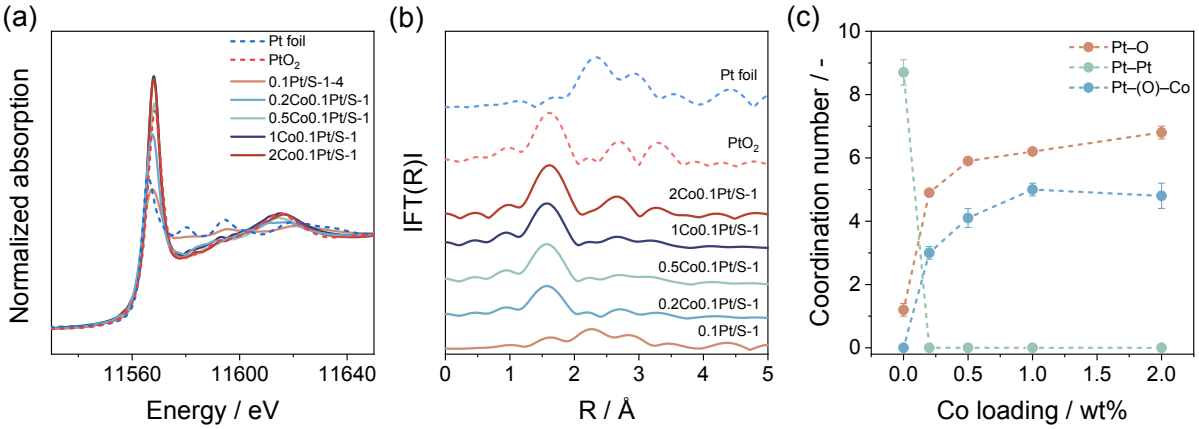

Fig. 3 Pt L_3-edge (a) XANES and (b) EXAFS spectra of 0.1Pt/S-1, xCo0.1Pt/S-1 (x = 0.2, 0.5, 1 and 2) and the reference samples (Pt foil and PtO_2). (c) Pt–O, Pt–Pt, and Pt–(O)–Co coordination numbers versus Co loading.

Fourier-transform (FT) k^2-weighted extended EXAFS analysis provided further insights into the coordination environment of Pt (Fig. 3b-c, Fig. S5, and Table S2). For the 0.1Pt/S-1 catalyst, a Pt–Pt coordination number of approximately 8.7 was obtained, characteristic of Pt aggregates or nanoparticles. In agreement with these experimental observations, our DFT calculations reveal a pronounced tendency of Pt atoms to aggregate. The analysis of Pt_n clusters (n = 2, 3, 6, and 13, Fig. S6a) shows that the average energy per Pt atom becomes more negative with increasing cluster size (Fig. S6b), indicating higher thermodynamic stability for larger clusters. This trend implies a strong driving force for Pt atoms to form larger clusters rather than remain as isolated species. On the other hand, the Pt–O contribution, with a coordination number of 1.2, suggests that a small fraction of surface Pt atoms remain connected to the support via Pt–O bonds. For the bimetallic catalysts (xCo0.1Pt/S-1), the Pt–(O)–Co coordination number increased from 3.0 to 5.0 with increasing Co content from 0.2 wt% to 1 wt% and then remained stable, suggesting strong interactions between Pt and CoO_x (Fig. 3c). To further understand these observations, DFT calculations were performed for PtO_2 interacting with the $Co_{12}O_{12}$ cluster. The results demonstrate that the incorporation of PtO_2 into the $Co_{12}O_{12}$ structure is significantly more favorable than its adsorption on the cluster surface, with a clear preference for the incorporation into the surface region over the bulk region (Fig. S7). These

findings provide a theoretical basis for the experimentally observed stabilization of Pt in an oxidized form within CoO_x-containing samples rather than as metallic aggregates.

Transmission electron microscopy (TEM) analysis was performed to gain insight into the distribution of supported species on the surface of the S-1 zeolite support. Despite the low loading of this metal, Pt nanoparticles were observed on the surface of 0.1Pt/S-1 (Fig. S8), which is consistent with the XAS results and DFT calculations. Only a very limited number of Co clusters were detected on the surface of the 1Co/S-1 catalyst, while EDS mapping reveals a uniform distribution of Co, indicating that Co species are highly dispersed (Fig. S9). Similarly, only a very limited number of small clusters were observed on the surface of the bimetallic 1Co0.1Pt/S-1 catalyst. EDS mapping reveals a homogeneous distribution of Pt, in sharp contrast to the distinct Pt nanoparticles observed on the surface of the 0.1Pt/S-1 catalyst, suggesting that the introduction of Co promotes the dispersion of Pt species (Fig. 4).

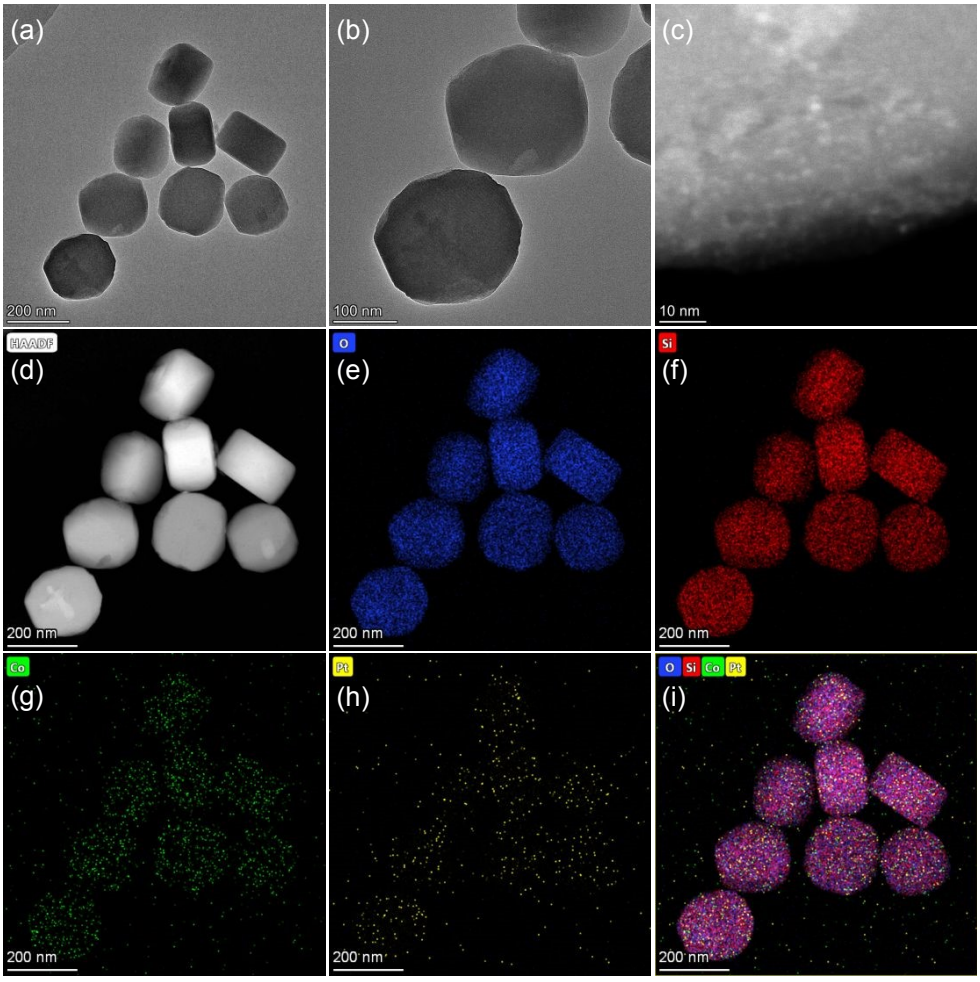

Fig. 4 (a-b) TEM images, (c-d) HAADF-STEM images, and (e-i) EDS mapping of the 1Co0.1Pt/S-1 catalyst.

Catalytic performance

The initial rate of propene formation was determined over all catalysts at 550 °C under differential reactor operation, with the propane conversion maintained below 10%. For the bimetallic xCo0.1Pt/S-1 catalysts, the rate shows a volcano-type trend with increasing Co loading, reaching a maximum value of 34 mmol g^{-1} min^{-1} at 1 wt% Co (Fig. 5a). When the Co loading is further increased to 2 wt%, the Pt–(O)–Co coordination number remains nearly unchanged (4.8), suggesting that the Pt–(O)–Co coordination number has reached a plateau and that further Co addition does not substantially increase the population of highly coordinated Pt-Co bimetallic sites. Moreover, the contribution of the additional Co species to the overall PDH activity is limited, as evidenced by the much lower activity of monometallic Co/S-1 catalysts. Excess Co species may also partially cover or hinder access to the highly active Pt-Co bimetallic sites, further reducing their effective accessibility and contributing to the observed decrease in activity above 1 wt% Co. Notably, the rate of these catalysts is significantly higher than the sum of the rates over the corresponding monometallic xCo/S-1 and 0.1Pt/S-1 catalysts (Fig. 5b and Fig. S10). The most significant increase in the rate, which was 15 times, was found for the 1Co0.1Pt/S-1 catalyst due to the presence of Pt and Co (Fig. 5b).

The substantial difference in the activity between mono- and bimetallic catalysts can be attributed to the formation of distinct active sites. This assumption is supported by the significantly lower apparent activation energy (E_a) of propene formation over the 1Co0.1Pt/S-1 catalyst (53 kJ mol^{-1}) compared with the monometallic 1Co/S-1 (104 kJ mol^{-1}) and 0.1Pt/S-1 (100 kJ mol^{-1}) catalysts (Fig. S11).

To assess the industrial potential of the most promising 1Co0.1Pt/S-1 catalyst, we tested this material in parallel with an analogue of the commercial $PtSn/Al_2O_3$ catalyst at industrially relevant degrees of propane conversion using a feed containing 40 vol% C_3H_8 in N_2 (Fig. 5c). Our catalyst achieved an initial propane conversion of 35.6%, which is approximately 83% of the equilibrium conversion. However, the reference catalyst exhibited only 7% initial propane conversion. Notably, the 1Co0.1Pt/S-1 catalyst also showed excellent on-stream stability, with propane conversion decreasing from 35.6% to only 32.8% during 12 h on stream, corresponding to an apparent deactivation rate constant (k_d) of 0.01 h^{-1}. In contrast, the $PtSn/Al_2O_3$ catalyst lost nearly all of its initial propane conversion within 4 h under the same reaction conditions.

We also benchmarked the 1Co0.1Pt/S-1 catalyst against the previously reported Pt-based catalysts in terms of space-time yield of propene formation, normalized either by the

overall catalyst amount ($STY(C_3H_6)_{cat}$) or by the Pt loading ($STY(C_3H_6)_{Pt}$). To ensure a proper comparison of catalysts tested under different reaction conditions, the $STY(C_3H_6)_{cat}$ and $STY(C_3H_6)_{Pt}$ values were plotted versus the ratio of the experimentally determined propane conversion to the corresponding equilibrium propane conversion ($X(C_3H_8)_{exp}/X(C_3H_8)_{eq}$). Our catalyst achieved a $STY(C_3H_6)_{cat}$ value of 15.6 kg_{C3H6} kg_{cat} h^{-1} at 83% of the equilibrium propane conversion (Fig. 5d and Table S3). This productivity level is among the top ten values. It should, however, be mentioned that the previously reported data was obtained at higher temperatures. Moreover, the intrinsic activity of PtCo species related to Pt, $STY(C_3H_6)_{Pt}$ value of 371 mol_{C3H6} g_{Pt} h^{-1}, stands out in comparison to those of the most previously reported Pt-containing catalysts tested under comparable or even higher temperatures (Fig. 5e). This result highlights the high efficiency of our catalysts in terms of using the expensive Pt for propane dehydrogenation.

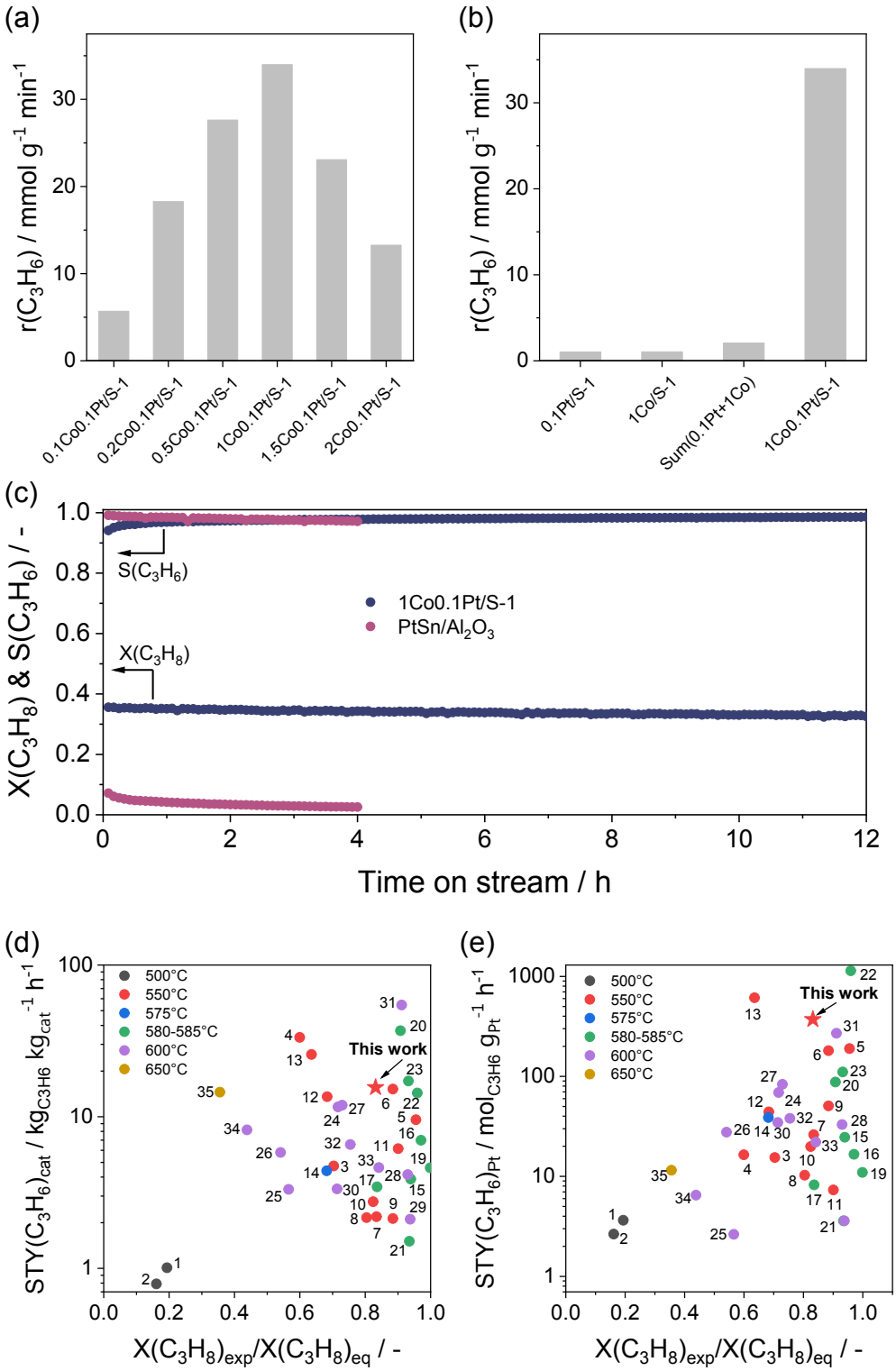

Fig. 5 (a) The initial propene formation rate over xCo0.1Pt/S-1 (x = 0.1, 0.2, 0.5, 1, 1.5, and 2). (b) The initial propene formation rate over 0.1Pt/S-1, 1Co/S-1, and 1Co0.1Pt/S-1, together with the summed rate of 0.1Pt/S-1 and 1Co/S-1. Reaction conditions for (a) and (b): T = 550 °C, WHSV(C_3H_8) = 94-752 h^{-1}, C_3H_8:N_2 = 2:3. (c) Time-on-stream profiles of propane conversion and propene selectivity over 1Co0.1Pt/S-1 and a commercial-like $PtSn/Al_2O_3$ catalyst. Reaction conditions: T = 550 °C, WHSV(C_3H_8) = 47 h^{-1}, C_3H_8:N_2 = 2:3. Comparison of (d) $STY(C_3H_6)_{cat}$ and (e) $STY(C_3H_6)_{Pt}$ for 1Co0.1Pt/S-1 and previously reported Pt-based catalysts (Table S3) at different temperatures as a function of $X(C_3H_8)_{exp}/X(C_3H_8)_{eq}$.

Structure-durability relationship

A typical drawback of various Pt-based catalysts is their inability to restore their initial performance in a series of dehydrogenation/regeneration cycles as required for commercial applications. This is due to the sintering of Pt species. Against this background, we also tested the bimetallic xCo0.1Pt/S-1 catalysts under alternating reaction conditions. As seen in Fig. 6a, the initial propane conversion over the 0.1Pt/S-1 catalyst decreased from 23% to 11% after the first oxidative catalyst regeneration. The catalyst became almost inactive after the second regeneration cycle, which was attributed to severe sintering of the Pt species, as evidenced by the increase in the Pt–Pt coordination number from 8.7 to 13.2 (Figs. S12-13 and Table S4). The durability improved with increasing Co loading in the xCo0.1Pt/S-1 catalysts. The catalysts with the loading of Co 1 wt% or higher practically fully restored their initial performance. This should be due to the stability of the supported bimetallic particles against sintering as exemplarily proven by TEM analysis of the spent 1Co0.1Pt/S-1 catalyst. No obvious Pt aggregation could be found after six dehydrogenation/regeneration cycles, while both Pt and Co remained homogeneously distributed throughout the S-1 support (Fig. S14). Thus, the presence of Co seems to inhibit Pt aggregation.

To quantitatively compare the durability of the developed catalysts, a regeneration efficiency factor was calculated as the ratio of the initial propane conversion in the last cycle to that obtained in the first cycle. The resulting values are shown in Fig. 6b. The regeneration efficiency increases from 0.04 for the 0.1Pt/S-1 catalyst to 0.94 with increasing Co loading from 0 to 1 wt% and remains essentially constant upon further increasing Co loading to 2 wt%. To rationalize the results in Fig. 6b, we correlated the regeneration efficiency of the catalysts with the Pt–(O)–Co coordination number of fresh catalyst, which serves as a descriptor of the interaction strength between Pt and Co. A clear positive correlation was observed (Fig. 6c), indicating that this initial material property is closely associated with the resistance of the bimetallic active sites to structural degradation during repeated dehydrogenation/regeneration cycles.

From a practical perspective, the simple impregnation procedure and ultralow Pt loading make it favorable to scale up the catalyst and reduce total costs. However, further improvement is required in terms of long-term durability, reproducible control of the Pt-Co local coordination during large-scale synthesis, and cost-effective production of the Silicalite-1 support for practical implementation.

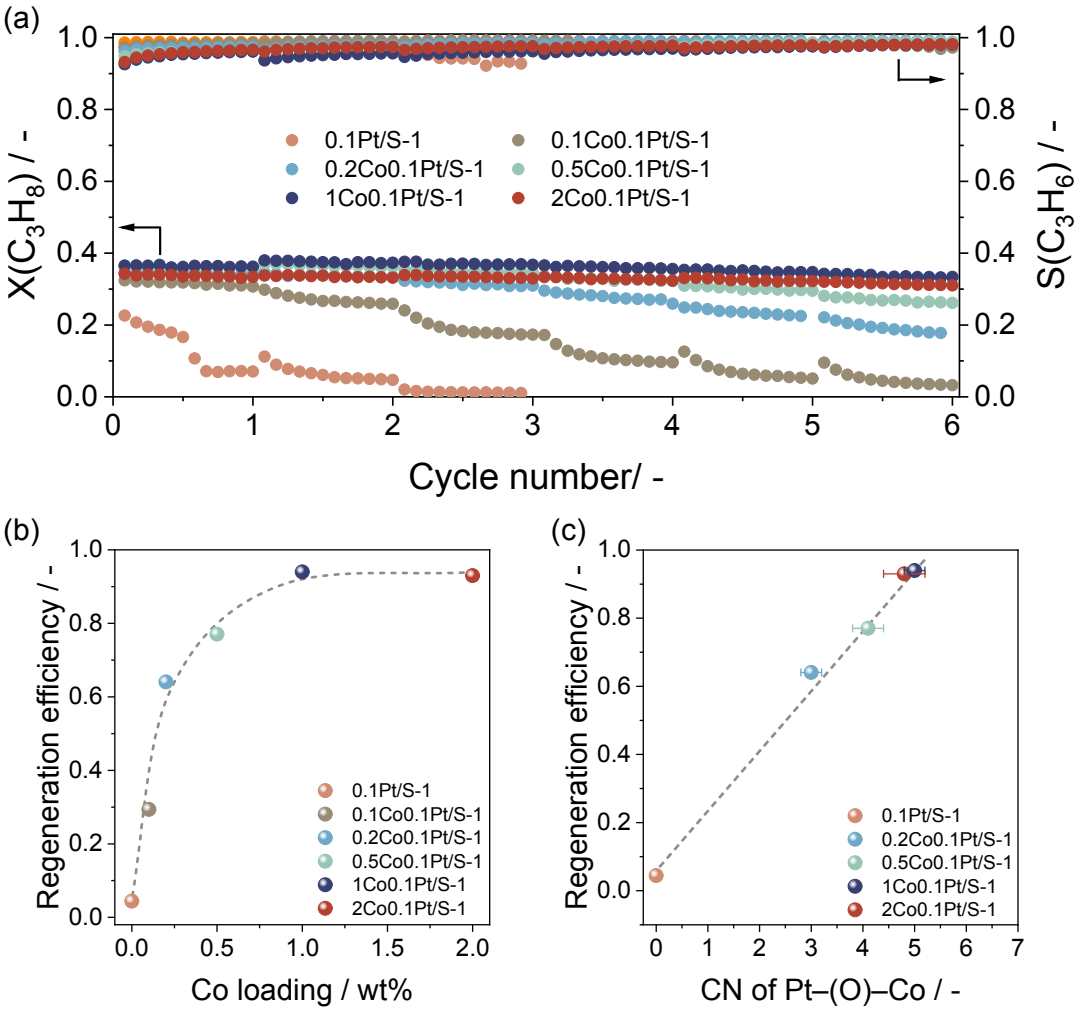

Fig. 6 (a) Propane conversion and propene selectivity over 0.1Pt/S-1 and xCo0.1Pt/S-1 (x = 0.1, 0.2, 0.5, 1, and 2) in a series of dehydrogenation/regeneration cycles. Reaction conditions: T = 550 °C, WHSV(C_3H_8) = 47 for xCo0.1Pt/S-1 and 7.1 h^{-1} for 0.1Pt/S-1, C_3H_8:N_2 = 2:3. Correlation of catalyst regeneration efficiency with (b) Co loading and (c) Pt–(O)–Co coordination number.

Conclusions

In summary, we provide fundamental insights into the synergistic effect of cobalt and platinum in S-1-supported CoPt bimetallic catalysts, containing tiny amounts of Pt, offering practical guidelines for the design of highly active and durable catalysts in the PDH reaction. This is achieved by combining catalytic tests in kinetic and industrially relevant regimes with sophisticated catalyst characterization using complementary state-of-the-art techniques and DFT calculations. In particular, the dispersion, local structure and electronic state of Pt are strongly affected by its interactions with CoO_x species. The DFT results suggest that Pt prefers to be stabilized on the surface of the CoO_x species rather than being incorporated into the bulk region, favoring the stabilization of oxidized Pt atoms. These features are essential for

reducibility of these species, a key step in creating highly active bimetallic $PtCoO_x$ species. The latter demonstrate an order-of-magnitude increase in propene formation rate compared to the monometallic species.

Moreover, the strength of the interactions between Pt and Co in the bimetallic species is affected by the Pt–(O)–Co coordination number. This controls the stability of the bimetallic species against sintering under alternating reducing and oxidizing conditions, which is advantageous for catalyst durability. Higher coordination numbers lead to higher durability. Whether analogous Pt–(O)–M coordination descriptors can be extended to other promoter metals remains an important topic for future investigation.

Data availability

The authors confirm that the data supporting the findings of this study are available within the article and its Supplementary Information.

Conflicts of interest

The authors declare no competing financial interest.

Acknowledgements

Financial support by the State of Mecklenburg-Vorpommern is gratefully acknowledged. We acknowledge DESY (Hamburg, Germany), a member of the Helmholtz Association HGF, for the prevision of experimental facilities. Parts of this research were carried out at PETRA III, and we would like to thank Dr. Edmund Welter for assistance in using beamline P65. Beamtime was granted for proposals I-20250490 and I-20250944.

References

1. T. Otroshchenko, G. Jiang, V. A. Kondratenko, U. Rodemerck and E. V. Kondratenko, *Chem. Soc. Rev.*, 2021, **50**, 473–527.
2. S. Chen, X. Chang, G. Sun, T. Zhang, Y. Xu, Y. Wang, C. Pei and J. Gong, *Chem. Soc. Rev.*, 2021, **50**, 3315–3354.
3. Y. Dai, X. Gao, Q. Wang, X. Wan, C. Zhou and Y. Yang, *Chem. Soc. Rev.*, 2021, **50**, 5590–5630.
4. A. H. Motagamwala, R. Almallahi, J. Wortman, V. O. Igenegbai and S. Linic, *Science*, 2021, **373**, 217–222.
5. Z. Xu, M. Gao, Y. Wei, Y. Yue, Z. Bai, P. Yuan, P. Fornasiero, J.-M. Basset, B. Mei, Z. Liu, H. Zhu, M. Ye and X. Bao, *Nature*, 2025, **643**, 691–698.
6. H. Hong, Z. Xu, B. Mei, W. Hu, P. Fornasiero, C. Wang, T. Wang, Y. Yue, T. Li, C. Yang, Q. Cui, H. Zhu and X. Bao, *Science*, 2025, **388**, 497–502.
7. J. J. H. B. Sattler, J. Ruiz-Martinez, E. Santillan-Jimenez and B. M. Weckhuysen, *Chem. Rev.*, 2014, **114**, 10613–10653.
8. Q. Zhang, M. Gao, V. A. Kondratenko, T. Otroshchenko, X. Ding, D. E. Doronkin, D. Wang, D. Li, D. Zhao and E. V. Kondratenko, *ACS Catal.*, 2026, **16**, 8915–8927.
9. Z. Xu, Y. Yue, X. Bao, Z. Xie and H. Zhu, *ACS Catal.*, 2020, **10**, 818–828.
10. L. Shi, G.-M. Deng, W.-C. Li, S. Miao, Q.-N. Wang, W.-P. Zhang and A.-H. Lu, *Angew. Chem. Int. Ed.*, 2015, **54**, 13994–13998.
11. Y. Nakaya, F. Xing, H. Ham, K.-i. Shimizu and S. Furukawa, *Angew. Chem. Int. Ed.*, 2021, **60**, 19715–19719.
12. B. Zhang, L. Zheng, Z. Zhai, G. Li and G. Liu, *ACS Appl. Mater. Interfaces*, 2021, **13**, 16259–16266.
13. R. Qian, S.-z. Luo, F. Jing and W. Fang, *Ind. Eng. Chem. Res.*, 2022, **61**, 17264–17274.
14. P. Wang, H. Liao, Y. Chen, X. Tao, Y. Gan, H. Deng, Y. Fu, Y. Tang, L. Wu and L. Tan, *ACS Catal.*, 2024, **14**, 8116–8129.
15. S. Chen, Z.-J. Zhao, R. Mu, X. Chang, J. Luo, S. C. Purdy, A. J. Kropf, G. Sun, C. Pei, J. T. Miller, X. Zhou, E. Vovk, Y. Yang and J. Gong, *Chem*, 2021, **7**, 387–405.
16. L. Xu, X. Tai, L. Feng, X. Zhang, Y. Pan, B. Tang, R. Xu, Y. Shui, J. Yuan, Y. Lin, X. Zhang, S. He, Z. Sun and S. Wei, *ACS Catal.*, 2025, **15**, 4172–4184.
17. L. G. Cesar, C. Yang, Z. Lu, Y. Ren, G. Zhang and J. T. Miller, *ACS Catal.*, 2019, **9**, 5231–5244.
18. X. Wang, C. Wu, J. Luo, K. Zhao, S. Zhang, Q. Jiang, S. Liang, Y. Zhao and Z. Gao, *J. Catal.*, 2026, **453**, 116490.
19. M. Numan, N. Sun Kim and C. Jo, *ChemNanoMat*, 2025, **11**, e202400527.
20. D. Xu, Q.-Y. Li, Q.-X. Su, S.-Y. Xia, Y.-S. Xu, B.-L. Leng, X. Lin, L.-Y. Fan, J.-S. Chen and X.-H. Li, *Angew. Chem. Int. Ed.*, 2025, **64**, e202419816.
21. D. Zhao, Y. Li, S. Han, Y. Zhang, G. Jiang, Y. Wang, K. Guo, Z. Zhao, C. Xu, R. Li, C. Yu, J. Zhang, B. Ge and E. V. Kondratenko, *iScience*, 2019, **13**, 269–276.
22. B. Ravel and M. Newville, *J. Synchrotron Radiat.*, 2005, **12**, 537–541.
23. P. E. Blöchl, *Phys. Rev. B*, 1994, **50**, 17953.
24. J. P. Perdew, K. Burke and M. Ernzerhof, *Phys. Rev. Lett.*, 1996, **77**, 3865.
25. G. Kresse and D. Joubert, *Phys. Rev. B*, 1999, **59**, 1758.
26. M. Thommes, K. Kaneko, A. V. Neimark, J. P. Olivier, F. Rodriguez-Reinoso, J. Rouquerol and K. S. W. Sing, *Pure Appl. Chem.*, 2015, **87**, 1051–1069.
27. J. Janas, T. Shishido, M. Che and S. Dzwigaj, *Appl. Catal. B Environ.*, 2009, **89**, 196–203.
28. L. Wu, Z. Ren, Y. He, M. Yang, Y. Yu, Y. Liu, L. Tan and Y. Tang, *ACS Appl. Mater. Interfaces*, 2021, **13**, 48934–48948.
29. Q. Zhang, V. A. Kondratenko, X. Ding, J. Weiss, S. Bartling, E. Fedorova, D. Zhao, D. E. Doronkin, D. Wang, C. Kubis and E. V. Kondratenko, *Chin. J. Catal.*, 2025, **74**, 108–119.
30. Y. Wang, H. Zhang, D. Han, M. Liu, B. He and Y. Zu, *Chem. Eng. J.*, 2025, **505**, 159514.
31. Q. Zhang, T. Zhang, B. Liu, E. Fedorova, D. E. Doronkin and E. V. Kondratenko, *Angew. Chem. Int. Ed.*, 2026, **65**, e19600.

32. Y. Li, Y. Ma, Q. Zhang, V. A. Kondratenko, G. Jiang, H. Sun, S. Han, Y. Wang, G. Cui, M. Zhou, Q. Huan, Z. Zhao, C. Xu, G. Jiang and E. V. Kondratenko, *J. Catal.*, 2023, **418**, 290–299.
33. C. H. Jung, J. Yun, K. Qadir, D. Park, J. Y. Yun and J. Y. Park, *Res. Chem. Intermed.*, 2016, **42**, 211–222.
34. Q. Zhang, Y. Li, X. Tian, V. A. Kondratenko, E. A. Fedorova, T. Yang, X. Ding, D. E. Doronkin, D. Zhao, C. Deng, H. Chen, S. Xu, A. Zanina, S. Bartling, T. Otroshchenko, Y. Wang, Z. Zhao, C. Xu, G. Jiang, H. Jiao and E. V. Kondratenko, *Nat. Catal.*, 2026, DOI: 10.1038/s41929-026-01488-w.

Data availability statement for

The authors confirm that the data supporting the findings of this study are available within the article and its Supplementary Information.